NANO LETTERS

pubs.acs.org/NanoLett Letter

# Imaging Dual-Moiré Lattices in Twisted Bilayer Graphene Aligned on Hexagonal Boron Nitride Using Microwave Impedance Microscopy

Xiong Huang,[†] Lingxiu Chen,[†] Shujie Tang, Chengxin Jiang, Chen Chen, Huishan Wang, Zhi-Xun Shen, Haomin Wang, and Yong-Tao Cui*

Cite This: *Nano Lett.* 2021, 21, 4292−4298 Read Online

ACCESS | Metrics & More | Article Recommendations | Supporting Information

**ABSTRACT:** Moiré superlattices (MSLs) formed in van der Waals materials have become a promising platform to realize novel two-dimensional electronic states. Angle-aligned trilayer structures can form two sets of MSLs which could potentially interfere. In this work, we directly image the moiré patterns in both monolayer and twisted bilayer graphene aligned on hexagonal boron nitride (hBN), using combined scanning microwave impedance microscopy and conductive atomic force microscopy. Correlation of the two techniques reveals the contrast mechanism for the achieved ultrahigh spatial resolution (<2 nm). We observe two sets of MSLs with different periodicities in the trilayer stack. The smaller MSL breaks the 6-fold rotational symmetry and exhibits abrupt discontinuities at the boundaries of the larger MSL. Using a rigid atomic-stacking model, we demonstrate that the hBN layer considerably modifies the MSL of twisted bilayer graphene. We further analyze its effect on the reciprocal space spectrum of the dual-moiré system.

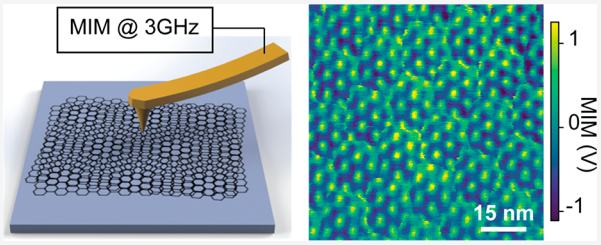


**KEYWORDS:** *microwave impedance microscopy, twisted bilayer graphene aligned on hBN, dual-moiré lattice, ultrahigh resolution (<2 nm)*



Stacking two layers of atomically thin materials of similar structures at a controlled alignment angle can form a moiré superlattice (MSL), whose periodicity could reach ten to hundreds of nanometers, much greater than those of individual atomic lattices. The periodic modulation in the MSL can induce drastic changes in the electronic structure of one or both layers, which has become a promising platform to explore novel electronic phases in two dimensions. For example, the MSL in a 0°-aligned monolayer graphene/hBN structure can induce secondary Dirac cones in the electronic band structure of the monolayer graphene, leading to a fractal structure in the Landau level spectrum, known as the Hofstadter's butterfly.[1−3] Twisted bilayer graphene with a magic angle around 1.1° can form flat minibands that host a strongly correlated Mott insulator and superconducting states.[4−6] This idea has further been realized in various versions of twisted graphene systems as well as angle-aligned bilayers of transition metal dichalcogenides, in which correlated insulating states, such as Mott insulator and generalized Wigner crystal phases, have been observed.[7−24] When a twisted bilayer graphene is further aligned on an hBN layer, ferromagnetism can be induced in this trilayer structure, and quantized anomalous Hall effect has also been observed, indicating the formation of a Chern insulator phase.[25,26] Multiple MSLs can potentially form in such aligned trilayer structures, contributing an extra degree of freedom for the electronic band engineering.[27−29]

Direct visualization of an MSL is of great importance in the characterization of its geometric structures. Spatially resolved techniques are ideal tools for this purpose as they can provide direct information in the real space. The large periodicity of the MSL has made it possible to image it with various scanning probe microscopy (SPM) techniques,[28,30−38] with the benefits of high throughput and relaxed requirements on sample preparations. Here, we report the observation of a dual-moiré pattern in a chemical vapor deposition (CVD) grown twisted bilayer graphene (TBG) that is aligned on an hBN substrate, using both scanning microwave impedance microscopy (MIM) and conductive atomic force microscopy (cAFM). Correlating results from these complementary imaging techniques pinpoints the tip−graphene contact resistance as the mechanism for the ultrahigh spatial resolution (better than 2 nm). In the TBG-hBN structure, two sets of MSLs are observed: a larger MSL (∼16 nm) due to the 0°-aligned graphene and hBN and a smaller MSL (3−6 nm) due to the

**Received:** February 10, 2021
**Revised:** April 28, 2021
**Published:** May 5, 2021

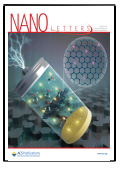





https://doi.org/10.1021/acs.nanolett.1c00601
*Nano Lett.* 2021, 21, 4292−4298

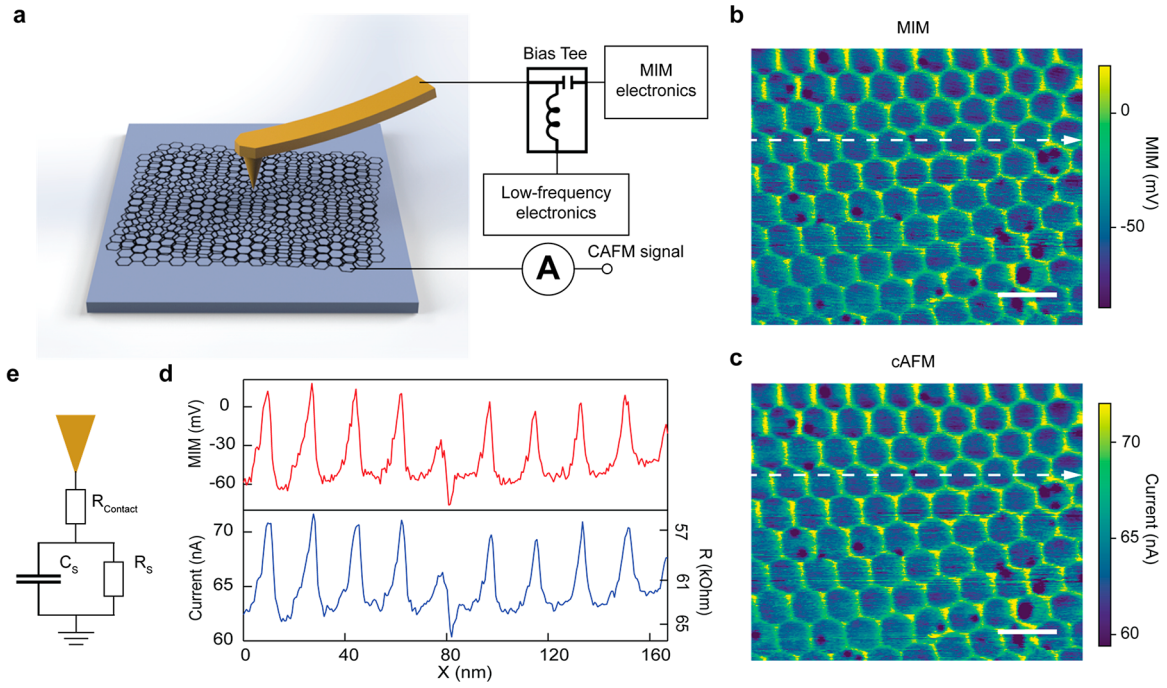


**Figure 1.** High-resolution imaging of moiré pattern in monolayer graphene/hBN sample. (a) Schematics of the experimental setup. (b and c) Simultaneously acquired (b) MIM and (c) cAFM images. (d) Linecuts extracted along the dotted lines in MIM and cAFM images. (e) Effective circuit model for the tip−graphene impedance probed in the contact mode MIM. $R_{contact}$ is the tip−sample contact resistance. $R_S$ and $C_S$ are the resistance and capacitance of the sample, respectively. Scale bars are 20 nm.

twisted graphene layers. Interestingly, the smaller MSL is distorted and exhibits abrupt discontinuities at the boundaries of the larger MSL. Using a simple atomic stacking model, these features can be recovered by considering all three layers in the formation of the moiré features. We further identify the signatures of the dual-moiré pattern on the reciprocal-space spectrum of the trilayer structure, which could potentially modify the electronic structure of the twisted bilayer graphene.

First, we demonstrate high-resolution MIM imaging of the MSL in monolayer graphene aligned on hBN. The schematics of the measurement is shown in Figure 1a. The moiré sample used in our study is grown by CVD method, in which a monolayer graphene grows epitaxially on an exfoliated hBN flake[33,34] (see Methods for more details). Therefore, the alignment angle is precisely 0°, which is expected to generate a moiré lattice with a periodicity of approximately 14 nm. In the MIM measurement, a shielded cantilever probe is in direct contact with the graphene. A microwave signal (around 3 GHz) is routed to the probe, and the reflected signal is demodulated to generate the MIM signals. Figure 1b plots a typical MIM image for a graphene/hBN MSL. It clearly resolves the honeycomb pattern expected for the MSL, with a spatial resolution better than 2 nm. The honeycomb pattern has noticeable distortions in different regions, which is likely due to local strains in the graphene flake formed during the high-temperature growth process. Fourier transform analysis reveals an average periodicity of ∼16 nm, corresponding to a tensile strain of ∼0.15% in the monolayer graphene.

It is worth noting that the ultrahigh spatial resolution is unprecedented in conventional MIM experiments, whose resolution is dominated by the tip size (typically around 50 nm).[39−41] Recently, two experiments have reported high resolution in MIM imaging of graphene moiré structures,[42,43] but the contrast mechanism for the tip−sample impedance has remained elusive. Reference 42 identified the formation of a sharp protrusion during the tip conditioning process. Reference 43 proposed that water meniscus or piezoelectric effect could be responsible for the high spatial resolution. Here, by correlating with simultaneous cAFM measurement (see Methods), we conclude that the MIM signal contrast is caused by the local variation of tip−sample contact resistance. Figure 1c plots the cAFM image obtained simultaneously with the MIM image in Figure 1b. These two images show strikingly similar patterns, and even fine features look almost identical as demonstrated in the example linecuts in Figure 1d. Such high degree of similarity indicates that the contrast mechanism for the MIM signal is the same as that for cAFM, i.e., the tip-graphene contact resistance. As illustrated in Figure 1e, when the tip is in good electrical contact with the graphene flake, a contact resistance forms at the tip−graphene junction, which allows the low-frequency current to flow through. It also contributes to the total tip−sample impedance at microwave frequency, which modulates the microwave reflection and produces the MIM signal contrast. The high spatial resolution is thus determined by the electrically conductive tip−sample contact interface which can be subnanometers in size depending on the contact quality.[44] We note that this regime of low tip−sample contact resistance is not readily achieved in typical MIM measurements in which the tip−sample electrical contact is usually dominated by a thin insulating spacer layer. As a result, the typical MIM response curves, obtained by modeling the tip−sample contact as a capacitance, do not apply to this case (see the Supporting Information for a comparison of the two effective circuit models). We would like to point out that, unlike cAFM, the MIM measurement does not require a counter electrode on the sample, making it more versatile to characterize moiré structures without going


https://doi.org/10.1021/acs.nanolett.1c00601
Nano Lett. 2021, 21, 4292−4298

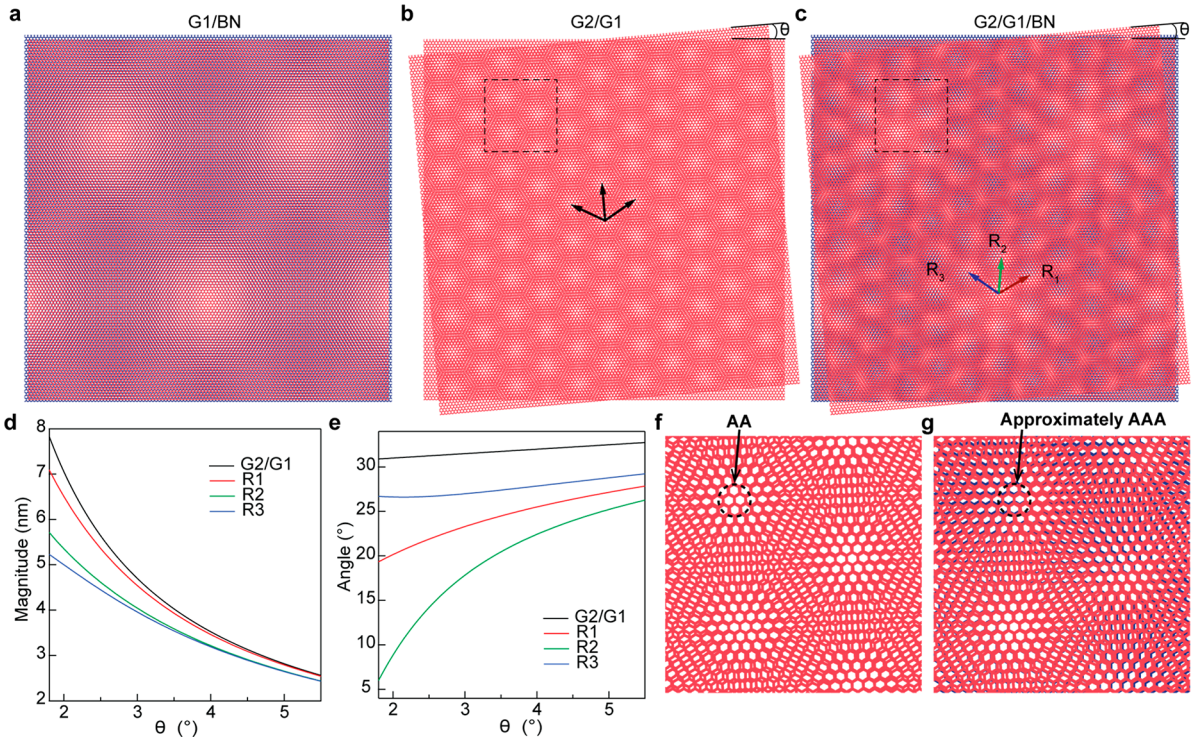


**Figure 2.** Analysis of the moiré patterns in a trilayer stacking. (a) 0°-aligned graphene/hBN. (b) Twisted bilayer graphene with a twist angle $\theta = 5°$. The black arrows correspond to the unit vectors of the moiré lattice. (c) Twisted bilayer graphene ($\theta = 5°$) on hBN with a 0° angle between G1 and hBN. The arrows labeled by R1-R3 correspond to the unit vectors of the small moiré lattice. (d and e) Magnitudes and orientations of the unit vectors in panels b and c. (f and g) Zoomed-in images for the regions indicated by the dotted squares in panles b and c, respectively.

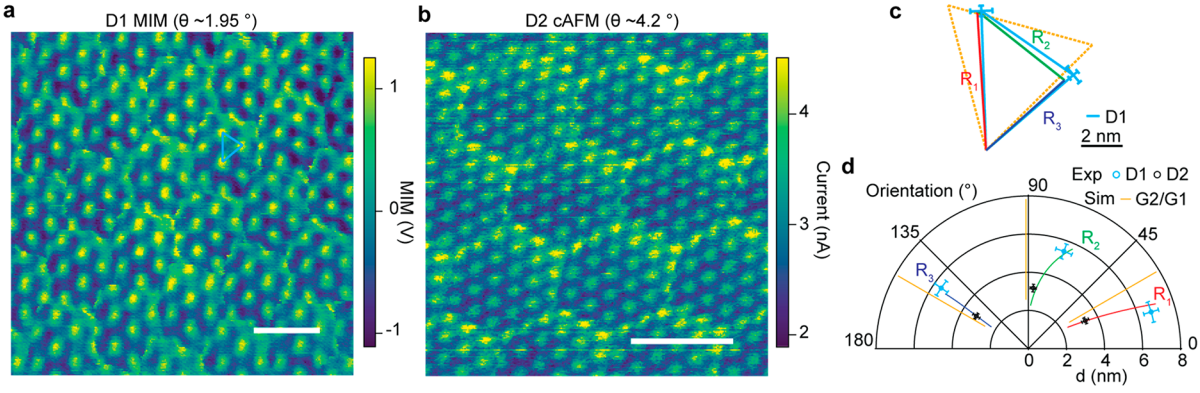


**Figure 3.** Imaging dual-moiré pattern in G2/G1/hBN trilayer stacking. (a) MIM image of a trilayer sample D1 with a 1.95° twist angle between G1 and G2. (b) cAFM image of a trilayer sample D2 with a 4.2° twist angle between G1 and G2. (c) Comparison of the unit vectors determined from experiment (device 1, cyan) and those from a trilayer stacking model (red, blue, and green) and a bilayer stacking model (orange dash). The error bars are determined from the uncertainties of the orientations of the moiré-L lattice in the experimental data. (d) Unit vectors of the moiré-S lattice for samples D1 and D2, compared with those calculated from a trilayer stacking model (R1, R2, and R3) and from a bilayer stacking model (G2/G1). Scale bars: (a and b) 15 nm and (c) 2 nm.

through extensive fabrication processes for making electrical leads.

Next, we explore the moiré superstructure formed in a trilayer stack in which a second graphene layer (G2) is stacked at an angle $\theta$ relative to the first graphene layer (G1) that has a 0° alignment on the hBN substrate. We expect two sets of moiré patterns: one from the 0° aligned G1 and hBN, and the other from G2/G1 with a twist angle $\theta$. We focus on the range $\theta \geq 1.8°$ so that the periodicity of the G2/G1 moiré is much smaller than that of G1/hBN (~14 nm), a scenario that has not been explored in previous studies which primarily focused on cases where the two moiré periodicities are similar.[27−29]

Figure 2 presents our analysis results based on a minimal model which simply considers the stacking of three rigid layers without any lattice relaxation or reconstruction. We find that the moiré pattern with a smaller periodicity (moiré-S) is divided into domains with a larger periodicity (moiré-L) (Figure 2c). Interestingly, while the two sets resemble the moiré patterns in individual bilayer structures of G2/G1 (Figure 2b) and G1/hBN (Figure 2a), it is not a simple combination of the two. There are two most notable features. First, the moiré-S pattern is along a different direction compared to the G2/G1 pattern with the same twist angle but without hBN. Second, the moiré-S pattern also has a


https://doi.org/10.1021/acs.nanolett.1c00601
Nano Lett. 2021, 21, 4292−4298

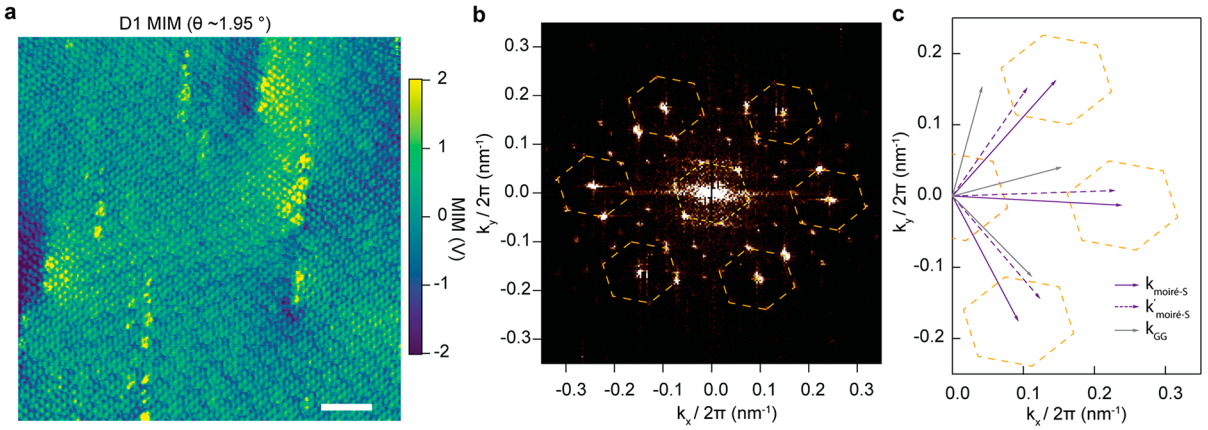


**Figure 4.** Analysis of the dual-moiré pattern in the reciprocal space. (a) MIM image of a large area in sample D1. Scale bar: 40 nm. (b) Fourier transform of the MIM image in panel a. The dotted hexagon centered at the origin corresponds to the moiré-L lattice, and the other hexagons are replicas centered at the peaks of the moiré-S lattice. (c) Comparison of the Fourier peaks of the moiré-S lattice extracted from panel b (solid purple arrows), the reciprocal vectors calculated from the moiré-S unit vectors determined from the real space data in D1 (Figure 3a) (dotted purple arrows), and the reciprocal vectors calculated for a twisted bilayer graphene with the same twist angle of 1.95° as D1 (gray arrows).

discontinuity near the domain boundary between two moiré-L hexagons. We further derive analytical expressions for the three unit vectors of moiré-S (see the Supporting Information). For each unit vector, we plot its magnitude and orientation with respect to the corresponding unit vector in G1 as a function of $\theta$ in panels d and e of Figure 2, respectively. We find that, compared to the G2/G1 moiré pattern in which the three unit vectors have equal magnitudes and are uniformly spaced at 60° apart (the black curves in Figure 2d,e), the moiré-S unit vectors have smaller and unequal magnitudes and their orientations are also significantly deviated from those in G2/G1, both of which are more pronounced at small twist angles. Such deviations from G2/G1 are due to the aligned hBN layer and can be readily seen in the analytical expressions presented in the Supporting Information. Simply speaking, it can be understood in the following way. Without the hBN layer, the center of each moiré-S hexagon corresponds to the AA stacking of the two graphene layers (Figure 2f). In the presence of the hBN layer, the center now should correspond to a nearly AAA stacking of three layers where the three A-site atoms are closest to each other (Figure 2g), which can be different from where the two A-site atoms from G1 and G2 are closest to each other.

We examine these model predictions experimentally by imaging the moiré superstructure in a twisted bilayer graphene aligned on the hBN substrate. The samples are grown by the same CVD method. During the growth, a second layer of graphene can grow on top of the first graphene layer at an angle that varies at different locations, which allows us to image moiré patterns of the G2/G1/hBN trilayer structure with many different twist angles between G2 and G1. Panels a and b of Figure 3 show two example images taken with MIM (Figure 3a) and cAFM (Figure 3b) in the contact mode (images of more samples of different twist angles are presented in Supporting Information). In each image, we can identify two periodic patterns of different length scales corresponding to the moiré-S and moiré-L patterns in the model. The moiré-S exhibits a triangular pattern of clear contrast with bright spots corresponding to a low tip−sample contact resistance. According to our analysis, these spots are the nearly AAA stacking regions of the trilayer structure. The moiré-L pattern is marked by boundaries of hexagon domains. These boundaries typically show an enhanced signal (a lower tip−sample contact resistance), and more strikingly, the moiré-S pattern has notable discontinuities at all moiré-L domain boundaries, exactly as expected from our model. To gain more quantitative comparisons, we analyze the unit vectors of the moiré-S patterns and plot them in a polar plot in Figure 3d, together with those calculated from our model. The measurement results agree well with model calculations. In particular, three unit vectors have unequal magnitudes and nonuniform angular spacings. These features are most pronounced in the case of Figure 3a, which has a larger periodicity corresponding to a smaller twist angle (Figure 3c). From Figure 3d, we further determine the twist angle for all the observed dual-moiré images, and the values range from 2° to 5° (see the Supporting Information).

Finally, we demonstrate the signatures of such a dual-moiré pattern in the reciprocal space, focusing on the effect of the discontinuity at the domain boundaries. We perform MIM imaging over a large area in the same region as the data in Figure 3a. The MIM image (Figure 4a) shows that the dual moiré pattern fills the entire area with only a few local variations in the signal intensity. We then perform fast Fourier transform (FFT) of the MIM image and plot the spectrum in Figure 4b. The spectrum contains a series of peaks which can be identified in the following categories. A dashed hexagon centered around the origin corresponds to the moiré-L pattern. Bright spots at large $k$ values correspond to the features from the moiré-S pattern. Because the moiré-S pattern is spatially modulated by the moiré-L boundaries, the moiré-L hexagon is further replicated at each of the bright spots in the moiré-S pattern. Other peaks are the higher-order peaks of these replica. To better illustrate their relation, we sketch only the main features in Figure 4c. We note that the moiré-S pattern contains the discontinuities at the moiré-L boundaries. To examine the effect of such discontinuities, we plot the reciprocal vectors ($k'_{\text{moiré-S}}$, labeled with dashed purple arrows) calculated directly from the unit vectors identified in Figure 3a. These $k$ vectors essentially represent the FFT peaks for a continuous moiré-S pattern without any modulation by the moiré-L pattern. Their positions significantly deviate from the experimentally obtained peak positions ($k_{\text{moiré-S}}$, labeled with solid purple arrows), and the differences are caused by the


https://doi.org/10.1021/acs.nanolett.1c00601
Nano Lett. 2021, 21, 4292−4298

discontinuities of the moiré-S pattern across the moiré-L domain boundaries, which are well-described by our analytical calculations presented in the Supporting Information.

Furthermore, we plot the $k_{GG}$ vectors (the gray arrows) corresponding to a twisted bilayer graphene with a twist angle of 1.95°, the same as that determined in the trilayer structure measured in Figure 4a. From the comparison of $k_{GG}$ with $k_{moiré\text{-}S}$ and $k'_{moiré\text{-}S}$, we identify the effect in the $k$-space structure of the twisted bilayer graphene due to the aligned hBN layer. As discussed in Figure 2, the aligned hBN layer changes the local moiré-S pattern by a small rotation as well as a distortion that breaks the original 6-fold rotational symmetry, which is reflected in the $k$-space as the change from $k_{GG}$ to $k'_{moiré\text{-}S}$. Then the discontinuities at the moiré-L boundaries further shift $k'_{moiré\text{-}S}$ to $k_{moiré\text{-}S}$. The $k$-space structure probed in our study reflects the spatial modulation of the tip−sample contact resistance which should correlate with the local electronic structure. Therefore, the aligned hBN layer could potentially modify the electronic structure of the twisted bilayer graphene in the momentum space. We believe our results could inspire further experimental and theoretical studies, such as band structure calculations, along these directions.

## METHODS

**Sample Preparation.** The graphene layers are deposited on exfoliated hBN flakes on quartz via chemical vapor deposition. The hBN flakes are mechanically exfoliated onto quartz and annealed at 600 °C in oxygen flow to remove residues. Then the quartz substrate with hBN is placed in a graphite tube and put into the CVD chamber. The growth of twisted bilayer graphene is carried out at 1300 °C. First, a mixture of ethyne and silane in pulsed flow is introduced to form the first polycrystalline graphene layer, and then the mixture is tuned to be in a stable flow to grow the second graphene layer. After that, the substrate cools slowly to room temperature. For the MIM measurement, the sample requires little preparation. For the cAFM measurement, an electrical contact is made to the polycrystalline graphene layer that is continuous in a large area, using silver epoxy in remote locations far from the tip scan regions.

**MIM and cAFM Measurements.** The MIM and cAFM measurements are performed on commercial atomic force microscopes (Bruker Dimension Icon AFM and Asylum Research Cypher AFM). Shielded MIM probes (ScanWave probes from PrimeNano with a spring constant of about 1 N/m) have been used in contact mode scans. In MIM measurement, a microwave excitation (about 0.01 mW at 3 GHz) is routed to the MIM probe. The reflected microwave signal is analyzed to extract the demodulated outputs as MIM signals. For combined MIM and cAFM measurements (such as Figure 1), an additional low-frequency AC voltage (5 mV at ∼7.4 kHz) is coupled through a microwave bias tee and applied to the MIM probe on top of the microwave signal. The current flowing through the tip−sample junction is amplified and recorded as the cAFM image. We have also performed standalone cAFM measurement (such as Figure 3b, applied DC voltage: 5−10 mV) using specialized cAFM probes (ASYELEC.01-R2 probes from Asylum Research with a spring constant of about 2.8 N/m), in which case only cAFM is measured.

## ASSOCIATED CONTENT

### Supporting Information

The Supporting Information is available free of charge at https://pubs.acs.org/doi/10.1021/acs.nanolett.1c00601.

MIM effective circuit models and response curves, data on additional samples (D2-D5), atomic stacking model for dual moiré structures, and FFT analysis of dual moiré patterns (PDF)

## AUTHOR INFORMATION


### Corresponding Author

**Yong-Tao Cui** − *Department of Physics and Astronomy, University of California, Riverside, California 92521, United States;* orcid.org/0000-0002-8015-1049; Email: yongtao.cui@ucr.edu

### Authors

**Xiong Huang** − *Department of Physics and Astronomy and Department of Materials Science and Engineering, University of California, Riverside, California 92521, United States;* orcid.org/0000-0003-2035-8387

**Lingxiu Chen** − *School of Materials Science and Physics, China University of Mining and Technology, Xuzhou 221116, China;* orcid.org/0000-0002-0820-7175

**Shujie Tang** − *2020 X-Lab, Shanghai Institute of Microsystem and Information Technology, Chinese Academy of Sciences, Shanghai 200050, China*

**Chengxin Jiang** − *State Key Laboratory of Functional Materials for Informatics, Shanghai Institute of Microsystem and Information Technology, Chinese Academy of Sciences, Shanghai 200050, China*

**Chen Chen** − *State Key Laboratory of Functional Materials for Informatics, Shanghai Institute of Microsystem and Information Technology, Chinese Academy of Sciences, Shanghai 200050, China*

**Huishan Wang** − *State Key Laboratory of Functional Materials for Informatics, Shanghai Institute of Microsystem and Information Technology, Chinese Academy of Sciences, Shanghai 200050, China*

**Zhi-Xun Shen** − *Department of Physics and Applied Physics, Geballe Laboratory for Advanced Materials, Stanford University, Stanford, California 94305, United States*

**Haomin Wang** − *State Key Laboratory of Functional Materials for Informatics, Shanghai Institute of Microsystem and Information Technology, Chinese Academy of Sciences, Shanghai 200050, China*

Complete contact information is available at: https://pubs.acs.org/10.1021/acs.nanolett.1c00601


### Author Contributions

†X.H. and L.C. contributed equally to this work. H.W., Z.-X.S., and Y.-T.C. initiated the research. L.C. performed the sample growth with assistance from C.J., C.C., and H.W.. X.H. performed the MIM measurement. X.H., L.C., and C.C. performed the cAFM measurements. S.T. carried out the initial MIM measurements on the graphene/hBN structure. Y.-T.C. and X.H. analyzed the data and wrote the manuscript with input from all authors.

### Notes

The authors declare the following competing financial interest(s): Z.-X.S. is a cofounder of PrimeNano Inc., which



https://doi.org/10.1021/acs.nanolett.1c00601
Nano Lett. 2021, 21, 4292−4298

licensed the MIM technology from Stanford for a commercial instrument.

The data sets generated and/or analyzed during this study are available from the corresponding author upon reasonable request.

## ■ ACKNOWLEDGMENTS

We thank Q. Li for help on cAFM measurements. X.H. and Y.-T.C. acknowledge support from NSF under award DMR-2004701; the Hellman Fellowship award; and the seed fund from SHINES, an EFRC funded by the U.S. Department of Energy (DOE), Basic Energy Sciences (BES) under Award Number SC0012670. The sample growth and fabrication work was supported by the National Key R&D program (Grant No. 2017YFF0206106), the Strategic Priority Research Program of Chinese Academy of Sciences (Grant No. XDB30000000), National Natural Science Foundation of China (Grant Nos. 51772317, 91964102, and 12004406), the Science and Technology Commission of Shanghai Municipality (Grant No. 20DZ2203600), and Soft Matter Nanofab (SMN180827) of Shanghai Tech University. S.T. acknowledges support from the National Natural Science Foundation of China (No. 11974370) and the Shanghai Rising-Star Program (A-type) (Grant No. 20QA1411000). Z.-X.S. acknowledges support from the Gordon and Betty Moore Foundation through Grant No. GBMF4546.

## ■ REFERENCES

(1) Ponomarenko, L. A.; Gorbachev, R. V.; Yu, G. L.; Elias, D. C.; Jalil, R.; Patel, A. A.; Mishchenko, A.; Mayorov, A. S.; Woods, C. R.; Wallbank, J. R.; Mucha-Kruczynski, M.; Piot, B. A.; Potemski, M.; Grigorieva, I. V.; Novoselov, K. S.; Guinea, F.; Fal'ko, V. I.; Geim, A. K. Cloning of Dirac fermions in graphene superlattices. *Nature* **2013**, *497*, 594−597.

(2) Yu, G. L.; Gorbachev, R. V.; Tu, J. S.; Kretinin, A. V.; Cao, Y.; Jalil, R.; Withers, F.; Ponomarenko, L. A.; Piot, B. A.; Potemski, M.; Elias, D. C.; Chen, X.; Watanabe, K.; Taniguchi, T.; Grigorieva, I. V.; Novoselov, K. S.; Fal'ko, V. I.; Geim, A. K.; Mishchenko, A. Hierarchy of Hofstadter states and replica quantum Hall ferromagnetism in graphene superlattices. *Nat. Phys.* **2014**, *10*, 525−529.

(3) Hunt, B.; Sanchez-Yamagishi, J. D.; Young, A. F.; Yankowitz, M.; LeRoy, B. J.; Watanabe, K.; Taniguchi, T.; Moon, P.; Koshino, M.; Jarillo-Herrero, P.; Ashoori, R. C. Massive Dirac Fermions and Hofstadter Butterfly in a van der Waals Heterostructure. *Science* **2013**, *340*, 1427−1430.

(4) Bistritzer, R.; MacDonald, A. H. Moire bands in twisted double-layer graphene. *Proc. Natl. Acad. Sci. U. S. A.* **2011**, *108*, 12233−12237.

(5) Cao, Y.; Fatemi, V.; Fang, S.; Watanabe, K.; Taniguchi, T.; Kaxiras, E.; Jarillo-Herrero, P. Unconventional superconductivity in magic-angle graphene superlattices. *Nature* **2018**, *556*, 43−50.

(6) Cao, Y.; Fatemi, V.; Demir, A.; Fang, S.; Tomarken, S. L.; Luo, J. Y.; Sanchez-Yamagishi, J. D.; Watanabe, K.; Taniguchi, T.; Kaxiras, E.; Ashoori, R. C.; Jarillo-Herrero, P. Correlated insulator behaviour at half-filling in magic-angle graphene superlattices. *Nature* **2018**, *556*, 80−84.

(7) Cao, Y.; Rodan-Legrain, D.; Rubies-Bigorda, O.; Park, J. M.; Watanabe, K.; Taniguchi, T.; Jarillo-Herrero, P. Tunable correlated states and spin-polarized phases in twisted bilayer−bilayer graphene. *Nature* **2020**, *583*, 215−220.

(8) Shen, C.; Chu, Y.; Wu, Q.; Li, N.; Wang, S.; Zhao, Y.; Tang, J.; Liu, J.; Tian, J.; Watanabe, K.; Taniguchi, T.; Yang, R.; Meng, Z. Y.; Shi, D.; Yazyev, O. V.; Zhang, G. Correlated states in twisted double bilayer graphene. *Nat. Phys.* **2020**, *16*, 520−525.

(9) Liu, X.; Hao, Z.; Khalaf, E.; Lee, J. Y.; Ronen, Y.; Yoo, H.; Haei Najafabadi, D.; Watanabe, K.; Taniguchi, T.; Vishwanath, A.; Kim, P. Tunable spin-polarized correlated states in twisted double bilayer graphene. *Nature* **2020**, *583*, 221−225.

(10) Chen, G.; Jiang, L.; Wu, S.; Lyu, B.; Li, H.; Chittari, B. L.; Watanabe, K.; Taniguchi, T.; Shi, Z.; Jung, J.; Zhang, Y.; Wang, F. Evidence of a gate-tunable Mott insulator in a trilayer graphene moiré superlattice. *Nat. Phys.* **2019**, *15*, 237−241.

(11) Chen, G.; Sharpe, A. L.; Gallagher, P.; Rosen, I. T.; Fox, E. J.; Jiang, L.; Lyu, B.; Li, H.; Watanabe, K.; Taniguchi, T.; Jung, J.; Shi, Z.; Goldhaber-Gordon, D.; Zhang, Y.; Wang, F. Signatures of tunable superconductivity in a trilayer graphene moiré superlattice. *Nature* **2019**, *572*, 215−219.

(12) Chen, G.; Sharpe, A. L.; Fox, E. J.; Zhang, Y.-H.; Wang, S.; Jiang, L.; Lyu, B.; Li, H.; Watanabe, K.; Taniguchi, T.; Shi, Z.; Senthil, T.; Goldhaber-Gordon, D.; Zhang, Y.; Wang, F. Tunable correlated Chern insulator and ferromagnetism in a moiré superlattice. *Nature* **2020**, *579*, 56−61.

(13) Chen, S.; He, M.; Zhang, Y.; Hsieh, V.; Fei, Z.; Watanabe, K.; Taniguchi, T.; Cobden, D. H.; Xu, X.; Dean, C. R.; Yankowitz, M. Electrically tunable correlated and topological states in twisted monolayer−bilayer graphene. *Nat. Phys.* **2021**, *17*, 374−380.

(14) Polshyn, H.; Zhu, J.; Kumar, M. A.; Zhang, Y.; Yang, F.; Tschirhart, C. L.; Serlin, M.; Watanabe, K.; Taniguchi, T.; MacDonald, A. H.; Young, A. F. Electrical switching of magnetic order in an orbital Chern insulator. *Nature* **2020**, *588*, 66−70.

(15) Xu, S.; Al Ezzi, M. M.; Balakrishnan, N.; Garcia-Ruiz, A.; Tsim, B.; Mullan, C.; Barrier, J.; Xin, N.; Piot, B. A.; Taniguchi, T.; Watanabe, K.; Carvalho, A.; Mishchenko, A.; Geim, A. K.; Fal'ko, V. I.; Adam, S.; Neto, A. H. C.; Novoselov, K. S.; Shi, Y. Tunable van Hove Singularities and Correlated States in Twisted Monolayer-bilayer Graphene. *Nat. Phys.* **2021**. DOI: 10.1038/s41567-021-01172-9.

(16) Wu, F.; Lovorn, T.; Tutuc, E.; MacDonald, A. H. H. Hubbard Model Physics in Transition Metal Dichalcogenide Moiré Bands. *Phys. Rev. Lett.* **2018**, *121*, 026402.

(17) Wang, L.; Shih, E.; Ghiotto, A.; Xian, L.; Rhodes, D. A.; Tan, C.; Claassen, M.; Kennes, D. M.; Bai, Y.; Kim, B.; Watanabe, K.; Taniguchi, T.; Zhu, X.; Hone, J.; Rubio, A.; Pasupathy, A. N.; Dean, C. R. Correlated electronic phases in twisted bilayer transition metal dichalcogenides. *Nat. Mater.* **2020**, *19*, 861−866.

(18) Xu, Y.; Liu, S.; Rhodes, D. A.; Watanabe, K.; Taniguchi, T.; Hone, J.; Elser, V.; Mak, K. F.; Shan, J. Correlated insulating states at fractional fillings of moiré superlattices. *Nature* **2020**, *587*, 214−218.

(19) Huang, X.; Wang, T.; Miao, S.; Wang, C.; Li, Z.; Lian, Z.; Taniguchi, T.; Watanabe, K.; Okamoto, S.; Xiao, D.; Shi, S.-F.; Cui, Y.-T. Correlated Insulating States at Fractional Fillings of the $WS_2$/$WSe_2$ Moiré Lattice. *Nat. Phys.* **2021**. DOI: 10.1038/s41567-021-01171-w.

(20) Regan, E. C.; Wang, D.; Jin, C.; Bakti Utama, M. I.; Gao, B.; Wei, X.; Zhao, S.; Zhao, W.; Zhang, Z.; Yumigeta, K.; Blei, M.; Carlström, J. D.; Watanabe, K.; Taniguchi, T.; Tongay, S.; Crommie, M.; Zettl, A.; Wang, F. Mott and generalized Wigner crystal states in WSe2/WS2 moiré superlattices. *Nature* **2020**, *579*, 359−363.

(21) Chu, Z.; Regan, E. C.; Ma, X.; Wang, D.; Xu, Z.; Utama, M. I. B.; Yumigeta, K.; Blei, M.; Watanabe, K.; Taniguchi, T.; Tongay, S.; Wang, F.; Lai, K. Nanoscale Conductivity Imaging of Correlated Electronic States in WSe2/WS2Moiré Superlattices. *Phys. Rev. Lett.* **2020**, *125*, 186803.

(22) Tang, Y.; Li, L.; Li, T.; Xu, Y.; Liu, S.; Barmak, K.; Watanabe, K.; Taniguchi, T.; MacDonald, A. H.; Shan, J.; Mak, K. F. Simulation of Hubbard model physics in WSe2/WS2 moiré superlattices. *Nature* **2020**, *579*, 353−358.

(23) Jin, C.; Regan, E. C.; Yan, A.; Iqbal Bakti Utama, M.; Wang, D.; Zhao, S.; Qin, Y.; Yang, S.; Zheng, Z.; Shi, S.; Watanabe, K.; Taniguchi, T.; Tongay, S.; Zettl, A.; Wang, F. Observation of moiré excitons in WSe2/WS2 heterostructure superlattices. *Nature* **2019**, *567*, 76−80.

(24) Shimazaki, Y.; Schwartz, I.; Watanabe, K.; Taniguchi, T.; Kroner, M.; Imamoğlu, A. Strongly correlated electrons and hybrid excitons in a moiré heterostructure. *Nature* **2020**, *580*, 472−477.



https://doi.org/10.1021/acs.nanolett.1c00601
*Nano Lett.* 2021, 21, 4292−4298

(25) Sharpe, A. L.; Fox, E. J.; Barnard, A. W.; Finney, J.; Watanabe, K.; Taniguchi, T.; Kastner, M. A.; Goldhaber-Gordon, D. Emergent ferromagnetism near three-quarters filling in twisted bilayer graphene. *Science* **2019**, *365*, 605−608.
(26) Serlin, M.; Tschirhart, C. L.; Polshyn, H.; Zhang, Y.; Zhu, J.; Watanabe, K.; Taniguchi, T.; Balents, L.; Young, A. F. Intrinsic quantized anomalous Hall effect in a moiré heterostructure. *Science* **2020**, *367*, 900−903.
(27) Wang, L.; Zihlmann, S.; Liu, M.-H.; Makk, P.; Watanabe, K.; Taniguchi, T.; Baumgartner, A.; Schönenberger, C. New Generation of Moiré Superlattices in Doubly Aligned hBN/Graphene/hBN Heterostructures. *Nano Lett.* **2019**, *19*, 2371−2376.
(28) Wang, Z.; Wang, Y. B.; Yin, J.; Tóvári, E.; Yang, Y.; Lin, L.; Holwill, M.; Birkbeck, J.; Perello, D. J.; Xu, S.; Zultak, J.; Gorbachev, R. V.; Kretinin, A. V.; Taniguchi, T.; Watanabe, K.; Morozov, S. V.; Anđelković, M.; Milovanović, S. P.; Covaci, L.; Peeters, F. M.; Mishchenko, A.; Geim, A. K.; Novoselov, K. S.; Fal'ko, V. I.; Knothe, A.; Woods, C. R. Composite super-moiré lattices in double-aligned graphene heterostructures. *Sci. Adv.* **2019**, *5*, No. eaay8897.
(29) Andelkovic, M.; Milovanović, S. P.; Covaci, L.; Peeters, F. M. Double Moiré with a Twist: Supermoiré in Encapsulated Graphene. *Nano Lett.* **2020**, *20*, 979−988.
(30) Luo, Y.; Engelke, R.; Mattheakis, M.; Tamagnone, M.; Carr, S.; Watanabe, K.; Taniguchi, T.; Kaxiras, E.; Kim, P.; Wilson, W. L. In situ nanoscale imaging of moiré superlattices in twisted van der Waals heterostructures. *Nat. Commun.* **2020**, *11*, 4209.
(31) Woods, C. R.; Britnell, L.; Eckmann, A.; Ma, R. S.; Lu, J. C.; Guo, H. M.; Lin, X.; Yu, G. L.; Cao, Y.; Gorbachev, R. V.; Kretinin, A. V.; Park, J.; Ponomarenko, L. A.; Katsnelson, M. I.; Gornostyrev, Y. N.; Watanabe, K.; Taniguchi, T.; Casiraghi, C.; Gao, H.-J.; Geim, A. K.; Novoselov, K. S. Commensurate-incommensurate transition in graphene on hexagonal boron nitride. *Nat. Phys.* **2014**, *10*, 451−456.
(32) Zhang, S.; Song, A.; Chen, L.; Jiang, C.; Chen, C.; Gao, L.; Hou, Y.; Liu, L.; Ma, T.; Wang, H.; Feng, X.; Li, Q. Abnormal conductivity in low-angle twisted bilayer graphene. *Sci. Adv.* **2020**, *6*, No. eabc5555.
(33) Tang, S.; Wang, H.; Zhang, Y.; Li, A.; Xie, H.; Liu, X.; Liu, L.; Li, T.; Huang, F.; Xie, X.; Jiang, M. Precisely aligned graphene grown on hexagonal boron nitride by catalyst free chemical vapor deposition. *Sci. Rep.* **2013**, *3*, 2666.
(34) Tang, S.; Wang, H.; Wang, H. S.; Sun, Q.; Zhang, X.; Cong, C.; Xie, H.; Liu, X.; Zhou, X.; Huang, F.; Chen, X.; Yu, T.; Ding, F.; Xie, X.; Jiang, M. Silane-catalysed fast growth of large single-crystalline graphene on hexagonal boron nitride. *Nat. Commun.* **2015**, *6*, 6499.
(35) Gallagher, P.; Lee, M.; Amet, F.; Maksymovych, P.; Wang, J.; Wang, S.; Lu, X.; Zhang, G.; Watanabe, K.; Taniguchi, T.; Goldhaber-Gordon, D. Switchable friction enabled by nanoscale self-assembly on graphene. *Nat. Commun.* **2016**, *7*, 10745.
(36) Sunku, S. S.; Ni, G. X.; Jiang, B. Y.; Yoo, H.; Sternbach, A.; McLeod, A. S.; Stauber, T.; Xiong, L.; Taniguchi, T.; Watanabe, K.; Kim, P.; Fogler, M. M.; Basov, D. N. Photonic crystals for nano-light in moiré graphene superlattices. *Science* **2018**, *362*, 1153−1156.
(37) Yu, Z.; Song, A.; Sun, L.; Li, Y.; Gao, L.; Peng, H.; Ma, T.; Liu, Z.; Luo, J. Understanding Interlayer Contact Conductance in Twisted Bilayer Graphene. *Small* **2020**, *16*, 1902844.
(38) Mcgilly, L. J.; Kerelsky, A.; Finney, N. R.; Shapovalov, K.; Shih, E.; Ghiotto, A.; Zeng, Y.; Moore, S. L.; Wu, W.; Bai, Y.; Watanabe, K.; Taniguchi, T.; Stengel, M.; Zhou, L.; Hone, J.; Zhu, X.; Basov, D. N.; Dean, C.; Dreyer, C. E.; Pasupathy, A. N. Visualization of moiré superlattices. *Nat. Nanotechnol.* **2020**, *15*, 580−584.
(39) Lai, K.; Kundhikanjana, W.; Kelly, M. a.; Shen, Z.-X. Nanoscale microwave microscopy using shielded cantilever probes. *Appl. Nanosci.* **2011**, *1*, 13−18.
(40) Cui, Y.-T.; Ma, E. Y.; Shen, Z.-X. Quartz tuning fork based microwave impedance microscopy. *Rev. Sci. Instrum.* **2016**, *87*, 063711.
(41) Scrymgeour, D. A.; Baca, A.; Fishgrab, K.; Simonson, R. J.; Marshall, M.; Bussmann, E.; Nakakura, C. Y.; Anderson, M.; Misra, S. Determining the resolution of scanning microwave impedance microscopy using atomic-precision buried donor structures. *Appl. Surf. Sci.* **2017**, *423*, 1097−1102.
(42) Lee, K.; Utama, M. I. B.; Kahn, S.; Samudrala, A.; Leconte, N.; Yang, B.; Wang, S.; Watanabe, K.; Taniguchi, T.; Altoé, M. V. P.; Zhang, G.; Weber-Bargioni, A.; Crommie, M.; Ashby, P. D.; Jung, J.; Wang, F.; Zettl, A. Ultrahigh-resolution scanning microwave impedance microscopy of moiré lattices and superstructures. *Sci. Adv.* **2020**, *6*, No. eabd1919.
(43) Ohlberg, D. A. A.; Gadelha, A. C.; Tamia, D.; Neto, E. G. S.; Miranda, D. A.; Lemos, J. S.; Santana, F. C.; Campos, L. C.; Ramírez, J. C.; Gonçalves do Rego, C.; Jorio, A.; Medeiros-Ribeiro, G. Observation of moiré superlattices on twisted bilayer graphene by scanning microwave impedance microscopy. *Proc. SPIE, Low-Dimensional Materials and Devices* **2020**, 114650J.
(44) Song, A.; Shi, R.; Lu, H.; Gao, L.; Li, Q.; Guo, H.; Liu, Y.; Zhang, J.; Ma, Y.; Tang, X.; Du, S.; Li, X.; Liu, X.; Hu, Y.-Z.; Gao, H.-J.; Luo, J.; Ma, T.-B. Modeling Atomic-Scale Electrical Contact Quality Across Two-Dimensional Interfaces. *Nano Lett.* **2019**, *19* (6), 3654−3662.


https://doi.org/10.1021/acs.nanolett.1c00601
*Nano Lett.* 2021, 21, 4292−4298